THE JOURNAL OF PHYSICAL CHEMISTRY B

Article

pubs.acs.org/JPCB

Frequency Distribution of the Amide-I Vibration Sorted by Residues in Amyloid Fibrils Revealed by 2D-IR Measurements and Simulations

Cyril Falvo,*[,†] Wei Zhuang,[‡] Yung Sam Kim,[§,⊗] Paul H. Axelsen,[∥] Robin M. Hochstrasser,[§] and Shaul Mukamel[⊥]

[†]Institut des Sciences Moléculaires d'Orsay, UMR CNRS 8214, Université Paris-Sud 11, 91405 Orsay, France

[‡]State Key Lab of Molecular Reaction Dynamics, Dalian Institute Chemical Physics, 457 ZhongShan Road, Dalian, LiaoNing, China, 116023

[§]Department of Chemistry, University of Pennsylvania, Philadelphia, Pennsylvania 19104-6323, United States

[⊗]School of Nano-Bioscience and Chemical Engineering, Ulsan National Institute of Science and Technology, Republic of Korea

[∥]Department of Pharmacology, Biochemistry and Biophysics, University of Pennsylvania School of Medicine, Philadelphia, Pennsylvania 19104-6084, United States

[⊥]Department of Chemistry, University of California Irvine, Irvine, California 92697-2025, United States

ABSTRACT: The infrared optical response of amyloid fibrils $A\beta_{1-40}$ is investigated. Simulations of two models corresponding to different protonation states are compared with experiment. The simulations reveal that vibrational frequency distributions inside the fibrils are dominated by side chain fluctuations. We further confirm earlier suggestions based on 2D-IR measurements that water molecules can be trapped inside the fibrils.

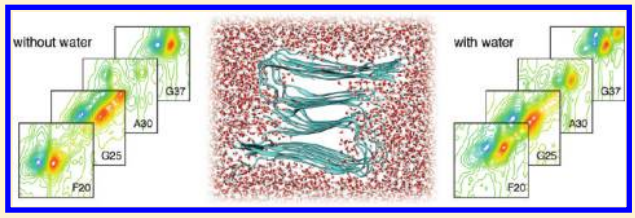

INTRODUCTION

The formation and deposition of amyloid fibrils is associated with more than 20 neurodegenerative diseases. These include Alzheimer's, Parkinson's, and Huntington's diseases, the transmissible spongiform encephalopathies, and type II diabetes.[1−5] Oligomeric or other prefibrillar precursors of the fibrils are believed to be the main toxic species, but the mechanism of cell and tissue damage in amyloid-related diseases is not well understood.[6] In the case of Alzheimer's disease, fibrils are composed of β-amyloid ($A\beta$) peptides ranging from 39 to 42 residues rich in β-sheet secondary structure. $A\beta$ fibrils are characterized by cross-β structural motifs, indicating that they are composed of β-strand segments nearly perpendicular to the long axes of the fibrils.[4,7] In the case of 40-residue β-amyloid ($A\beta_{1-40}$), Tycko and co-workers used solid-state NMR data to build detailed molecular models, which are in agreement with atomic force microscopy and electron microscopy.[8−12] These models show that residues 1−9 are structurally disordered, residues 10−24 and 30−40 form β-strands leading to in-register, parallel β-sheets, and residues 25−29 form a bend or a loop.[8−11] Depending on the experimental conditions, various morphologies of amyloid fibrils, which differ mainly by their overall symmetry and quaternary structure, are observed.[12] A 2-fold symmetry structure associated with untwisted, "striated ribbon" morphologies[10] and a 3-fold symmetry structure associated with "twisted pair" morphologies[12] were built.

This study focuses on the 2-fold symmetry structure. Such structures have been studied by Hummer and co-workers using molecular dynamics (MD).[13,14] They found that all models are stable at room temperature, and converge toward an interdigitated side chain packing for intermolecular contacts within and between the two-peptide units of the protofilaments.

Femtosecond nonlinear two-dimensional infrared (2D-IR) spectroscopy has proven to be a very powerful tool for probing the properties of biological systems, particularly peptides, proteins, membranes, and amyloid fibrils in the amide-I or amide-A frequency range.[15−35] In a 2D-IR photon echo experiment, three femtosecond pulses interact with the molecule to generate a signal that depends on two coherences. The signal is recorded as a function of the two time intervals over which these coherences are allowed to evolve. 2D-IR is therefore more powerful than classical linear techniques that involved only one coherence. It has femtosecond resolution and can bring new insights on the fast biological processes. It is also sensitive to the linear and nonlinear couplings between vibrational modes, which can bring additional information on the structure and dynamics. Finally, photon-echo spectra are usually spectrally narrower, much freer from background, and better resolved than linear spectra.

Isotope editing techniques allow a simplification of complex and overlapping features. For example, the substitution of $^{12}C{=}^{16}O$ by $^{13}C{=}^{18}O$ of a specific residue of a protein shifts the amide-I transition of the selected peptide bond away from the main amide-I band where vibrations are strongly coupled

Received: October 7, 2011
Revised: February 2, 2012
Published: February 16, 2012

dx.doi.org/10.1021/jp2096423 | J. Phys. Chem. B 2012, 116, 3322−3330

and delocalized. This protocol provides a particularly useful approach for probing the local properties of a system.

Extensive isotope-edited 2D-IR photon-echo of Aβ40 mature fibrils were reported recently.[19−21] Isotope labeling of a specific residue shifts the corresponding amide-I transitions for all strands. The assembly of strands forms a linear exciton chain of labeled amide units, which has an absorption frequency that is red-shifted by the intermolecular coupling.[20] The 2D-IR spectra of these linear chains have been measured for 18 residues located between Val12 and Val39.[19] This extensive data set provides local information on the amide-I vibrational dynamics inside the amyloid fibrils. The experiment was realized on amyloid fibrils with a morphology slightly different from the morphology of those studied by Tycko and co-workers.[10] Nevertheless, in the present study we will use the molecular model of Tycko to interpret the 2D-IR measurements. The goal of our study is to connect the 2D-IR measurements to the molecular structure. In section 2 we describe the MD simulations. Simulations of the frequency distributions are described in section 3. Finally, 2D-IR experimental and simulated spectra are reported in section 4.

MOLECULAR DYNAMICS SIMULATIONS

We have used the fragment Aβ_{9-40} of Aβ_{1-40} since it is known that residues 1−8 are structurally disordered and are not important for fibril growth.[11,13] Moreover, due to its disordered geometry, we assumed that it does not strongly influence the absorption properties of the rest of the monomer. To avoid a positive charge near the N-terminal side, which could influence the absorption spectra, we have added an acetamide group CH_3−C═O, before the residue Gly9.

To reveal the influence of the side chain protonation state on the spectra, we have studied two systems. S1 is Aβ_{9-40} with side chains Glu11, Glu22, and Asp23 negatively charged, and S2 is Aβ_{9-40} with side chains Asp and Glu neutral. Both systems were generated from the 2-fold symmetry NMR minimized structure Aβ_{9-40} computed in ref 10 and displayed in Figure 1. Using the

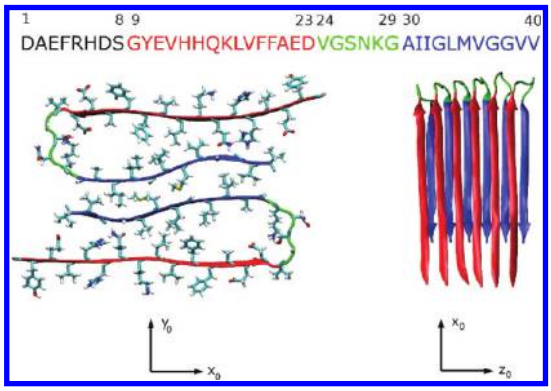

Figure 1. Aβ_{1-40} sequence and Aβ_{9-40} molecular model described in ref 10. The fibril axis is along z_0.

notation introduced in ref 10, our simulations were started from the STAG(+2) structure composed of 12 Aβ_{9-40} monomers (see Figure 2a). All simulations were performed using the NAMD 2.7 program[36] with the CHARMM27 force field.[37] Periodic boundary conditions with a 1 fs time step were used. Long-range electrostatic interactions were computed using particle-mesh Ewald (PME),[38,39] and a real space cutoff of 12 Å was used for nonbonded interactions. Langevin dynamics with a 1 ps damping coefficient were used to achieve a constant temperature. A constant 1 atm pressure was maintained using a Nose−Hoover Langevin piston[40,41] with a decay period of 200 fs and a 100 fs damping time.

To obtain minimized structures, a set of restraints on interpeptide hydrogen bonds length, backbone torsion angle, and side chain distances was used in ref 10. However, these restraints did not include the periodic boundary conditions. The drawback of using periodic boundary conditions on a small aggregate (six monomers along the fibril axis) is that it induces the loss of torsion, which has been observed experimentally and simulated as well.[13] However, to ensure the stability of the molecular structure during our simulation, the use of periodic boundary conditions is necessary. In a first step we have used the same hydrogen bond length and backbone torsion angle restraints used in ref 10 and run a 200 ps simulation to obtain a proper periodic structure (see Figure 2b). During this simulation, only the box size along the z_0 axis (fibrils axis, see Figure 1) is allowed to vary. Restraints are implemented using the colvars module, part of the NAMD 2.7 program, and include backbone torsion angle for residues 10−12, 15−21, 30−32, 34−36, and 39 (Φ = −150°, Ψ = 150°, 0.01 kcal/mol·deg^2 force constants) and backbone hydrogen bond distance for residues 10−24 and 30−40 (2.15 Å oxygen−hydrogen distances, 10.0 kcal/mol·Å^2 force constants).

For both S1 and S2, the amyloid is included in a TIP3 water box[42] containing 9309 and 9266 water molecules, respectively (see Figure 2c). Water molecules were allowed to penetrate into the fibrils. For system S2, 36 chloride ions were added to neutralize the box. Water and ions were equilibrated for 1 ns, while the fibril atoms were held fixed by harmonic restraints resulting in a box size of approximately 105 × 95 × 32 Å^3. After equilibration, all restraints were released and the systems were simulated for 25 ns at constant pressure and temperature. During the first 1 ns, the systems relax and tend to get more compact. As a result, the box size along the fibril axis reduces to approximately 30 Å. This value indicates an interpeptide distance of 5 Å, typical of β-sheets. The box size of the system after 1 ns is approximately 110 × 100 × 30 Å^3.

The average C_α root-mean-square deviation (rmsd) is shown as a function of time in Figure 3 from the time t = 0 where all constraints were released. The rmsd value was computed for each time by comparing the fluctuating structure to the initial structure taken from ref 10 (Figure 3). At each time step, the structure was aligned and reoriented to adjust to the reference structure. At t = 0, the C_α rmsd is 2.5 Å for S1 and 2.8 Å for S2. The nonvanishing C_α rmsd is due the periodic boundary conditions imposed on our system, and the system is already modified at t = 0. For S2, the C_α rmsd increases, reaching an average value of 3.5 Å. For S1, the rmsd keeps increasing slowly over the range of our simulation; however, no strong perturbation in the structure was observed (see Figure 2d). This indicates that while S2 is stable over our simulation, S1 is slowly changing. To save computational cost and to better compare systems S1 and S2, we assumed that the slow variation over system S1 does not strongly modify the amide-I vibrational dynamics, and it was neglected.

FREQUENCY CALCULATIONS

Each peptide bond along the amyloid fibrils contains an amide-I vibration. In this section, we provide a detailed description of the calculation of the amide-I vibrational frequencies and their corresponding fluctuations. Several models have been used in

dx.doi.org/10.1021/jp2096423 | J. Phys. Chem. B 2012, 116, 3322−3330

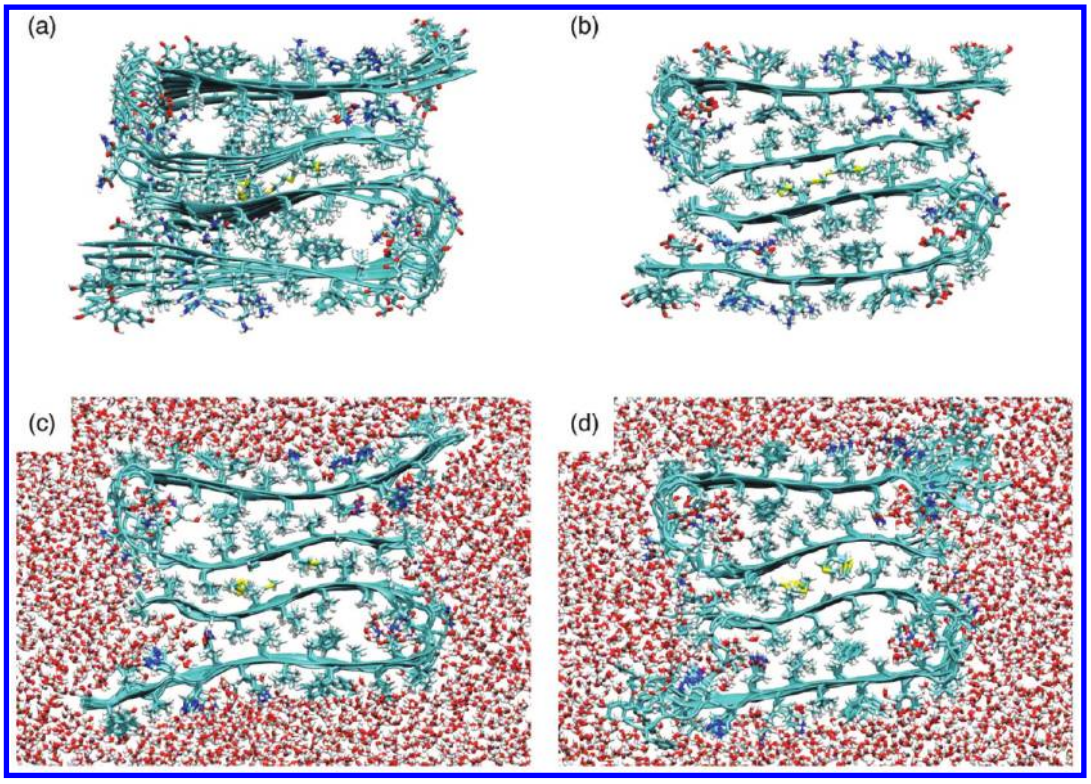

Figure 2. (a) Initial structure of Aβ_{9-40} taken from ref 10. (b) System S1: modified constrained structure using periodic boundary conditions. (c) System S1: solvated structure at t = 0 when constraints are released. (d) System S1: solvated structure at t = 10 ns.

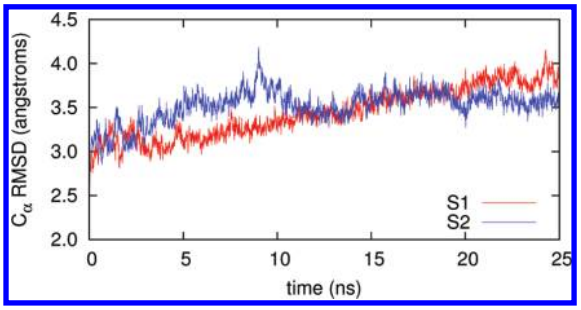

Figure 3. Backbone C$_\alpha$ rmsd's from the initial structure (ref 10).

the past to accomplish this goal. In order to establish a link between structure fluctuations and the frequencies, DFT maps were recently introduced by combining *ab initio* calculations and MD simulated trajectories.[43−55] Several parametrization schemes have been employed for the amide I mode in peptides.[43−49,51,52] We have used the CHO4 parametrization.[43−45] This is based on the expansion of the vibrational frequency as a linear combination of the electrostatic potential computed at the 4 coordinates of the atoms C, O, N, and H of each amide bond. The amide-I vibrational frequency of the nth peptide bond located between residue r and r + 1 of the monomer α is written as

$$\hbar\omega_{\alpha,n} = \hbar\omega_0 + \sum_s l_s \phi_{\alpha,n,s}(t) \tag{1}$$

The sum is performed over the C, O, N, and H atoms of the peptide bond n. The coefficients l_s are given by $l_C = -0.00554e$, $l_O = 0.00160e$, $l_N = 0.00479e$, $l_H = -0.00086e$, where e is the electronic charge. The electrostatic potential $\phi_{\alpha,n,s}(t)$ calculated at the $\mathbf{r}_{\alpha,n,s}(t)$ coordinate of the atom s of the nth peptide bond of monomer α is expressed as the sum of different contributions

$$\phi_{\alpha,n,s}(t) = \phi^{\text{water}}_{\alpha,n,s}(t) + \phi^{\text{backbone}}_{\alpha,n,s}(t) + \phi^{\text{side chains}}_{\alpha,n,s}(t) \tag{2}$$

$\phi^{\text{water}}_{\alpha,n,s}(t)$ corresponds to the electrostatic potential generated by the surrounding water molecules and is computed using the TIP3[42] point charges.

$$\phi^{\text{water}}_{\alpha,n,s}(t) = \frac{1}{4\pi\varepsilon_0} \sum_{i\in W} \frac{q_i}{|\mathbf{r}_i(t) - \mathbf{r}_{\alpha,n,s}(t)|} \tag{3}$$

where $\mathbf{r}_i(t)$ are the coordinates of the charge i. The sum is performed over all water point charges W. $\phi^{\text{backbone}}_{\alpha,n,s}(t)$ corresponds to the contribution generated by the amyloid fibril backbone atoms. In the backbone we include the atoms C, O, N, H, C$_\alpha$, and H$_\alpha$, and its contribution can be written as

$$\phi^{\text{backbone}}_{\alpha,n,s}(t) = \frac{1}{4\pi\varepsilon_0} \sum_{i\in B} \frac{q_i}{|\mathbf{r}_i(t) - \mathbf{r}_{\alpha,n,s}(t)|} \tag{4}$$

where the sum is performed over the set of point charges B. We have used two models for the backbone contribution. In the first model denoted B1, we considered the point charges taken from the CHARMM27 force field outside a certain range of the peptide bond. The excluded atoms of peptide bond n located between residue r and r + 1 are all the backbone charges of residue r and atoms N, H, C$_\alpha$, and H$_\alpha$ of residue r + 1 (see Figure 4). This model has previously been used to model the absorption of an α-helix with a different parametrization based on the electrostatic field and several derivatives.[51] The second model B2 follows the work of Ham et al.,[44,45] who compared ab initio and map frequency shift. The effective partial charges of

dx.doi.org/10.1021/jp2096423 | J. Phys. Chem. B 2012, 116, 3322−3330

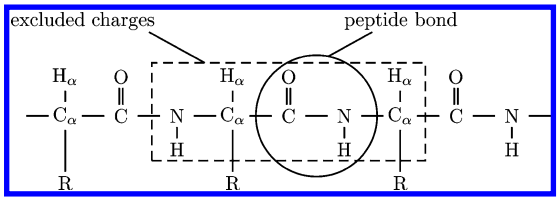

Figure 4. Excluded atoms for backbone contribution calculation of model B1. R designates the side chains.

the C, O, N, and H atoms of each peptide bond seen by the others were fitted to reproduce the ab initio calculations. No effectives charges are assigned to the C_α and H_α atoms. That study had found a good agreement between ab initio calculations and map if the following charge were used: q_C = 0.419, q_O = −0.871, q_N = 0.793, q_H = −0.341. Finally $\phi_{\alpha,n,s}^{\text{side chains}}(t)$ correspond to the side chains contribution and can be written as

$$\phi_{\alpha,n,s}^{\text{side chains}}(t) = \frac{1}{4\pi\varepsilon_0}\sum_{i\in S}\frac{q_i}{|\mathbf{r}_i(t) - \mathbf{r}_{\alpha,n,s}(t)|} \tag{5}$$

where the sum i is performed over all the side chains charges given by the CHARMM27 force field. Since the vibrational frequencies are proportional to the electrostatic potential, each contribution described previously induce a independent frequency shift whose sum gives the total frequency shift compared to the bare frequency ω_0 so that $\omega_{\alpha,n}(t)$ can be written as

$$\omega_{\alpha,n}(t) = \omega_0 + \Delta\omega_{\alpha,n}^{\text{water}}(t) + \Delta\omega_{\alpha,n}^{\text{backbone}}(t) + \Delta\omega_{\alpha,n}^{\text{side chains}}(t) \tag{6}$$

To properly account for periodic boundary conditions and the long-range interactions, we have used the PME method of Essmann and co-workers[38] to compute the electrostatic potential. The sum of the Coulombic interactions is split into two parts: short-range and long-range. The short-range is treated with a sum in Cartesian space and the long-range is treated with a reciprocal sum in Fourier space. In PME, the reciprocal sum is approximated by a discrete convolution on an interpolating grid using the fast Fourier transform. In our simulation, we used a cutoff of 16 Å to split long-range and short-range interactions. For the reciprocal sum, we use a sixth order B-spline interpolation and a mesh grid smaller than 1 Å. This allowed for full convergence of the electrostatic properties. Vibrational frequencies were computed every 10 ps for a total of 1000 snapshots using the last 10 ns of our MD simulation. This yields the fluctuating shift created by each contribution: backbone, side chains, and water for each peptide bond of each residue. To analyze this extended data set we have computed the average frequency shift and standard deviation of each residue:

$$\langle\Delta\omega_n\rangle = \langle\Delta\omega_{\alpha,n}(t)\rangle_{\alpha,t} \tag{7}$$

$$\sigma(\Delta\omega_n) = \sqrt{\langle\Delta\omega_{\alpha,n}^2(t)\rangle_{\alpha,t} - \langle\Delta\omega_{\alpha,n}(t)\rangle_{\alpha,t}^2} \tag{8}$$

where $\langle\ldots\rangle_{\alpha,t}$ denotes a time average and an average over the different monomers resulting in a total of 12 000 samples. This amount of samples is enough to converge the first two moments: the average and the standard deviation.

Figure 5 depicts the average frequency shift and the corresponding standard deviation due to the water molecules

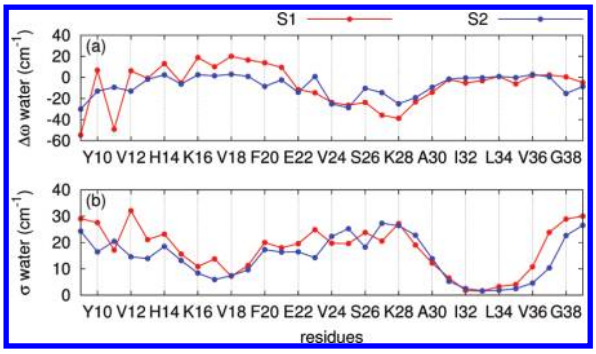

Figure 5. Average frequency shift (a) and corresponding standard deviation (b) due to the water molecules for all amide-I local modes along the peptide. (red line) system S1; (blue line) system S2.

for models S1 and S2. We first notice that the two curves S1 and S2 have a vanishing average frequency shift and standard deviation between the residues Ala30 and Val36. This can be explained by the fact that these residues are confined inside the 2-fold symmetry of the amyloid fibrils isolated from any water molecules (see Figure 2). $\langle\Delta\omega\rangle$ is smaller in the "protected" areas of the amyloid fibrils, ca. in the β-sheets between residues His13 and Ala21 and between residues Ala30 and Val36. Stronger fluctuations and average frequency shift are observed in the regions between residues Gly9 to Val12, Glu22 to Gly29, and Gly37 to Val39. These areas correspond to the tip of the monomers and the loop region.

In Figure 6 we display $\langle\Delta\omega\rangle$ and σ due to the backbone only for S1 and S2 using models B1 and B2. All frequency shifts have

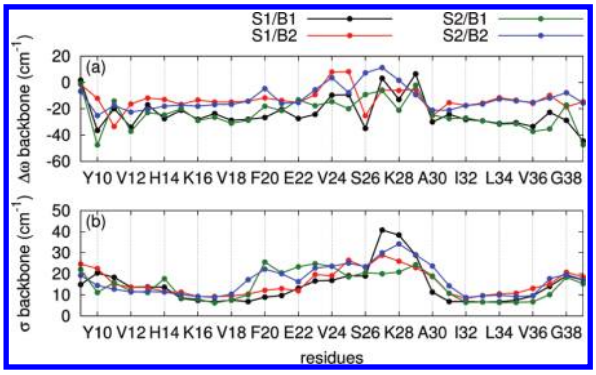

Figure 6. Average frequency shift (a) and corresponding standard deviation (b) due to the backbone only for all amide-I local modes along the peptide. (black line) system S1 and model B, (red line) system S1 and model B2, (green line) system S2 and model B1, (blue line) system S2 and model B2.

a similar behavior: $\langle\Delta\omega\rangle$ is rather flat in the β-sheet areas ($\approx$ −20 cm^{-1}) with small fluctuations ($\approx$ 10 cm^{-1}), while in the loop region the fluctuations of the frequency shift are much larger ($\approx$ 20−40 cm^{-1}). On the N-terminal side, the frequency shift tends to vanish and on both end, the standard deviation increases. The differences between S1 and S2 (for both B1 and B2) are observed in the loop region. This indicates some significant structural differences between the two systems in this area. In general, the shift computed from model B1 is larger than the shift computed from model B2. However, the general

dx.doi.org/10.1021/jp2096423 | J. Phys. Chem. B 2012, 116, 3322−3330

behavior remains the same. We also notice a lower average shift on the C-terminal side for model B1. This is due to the negative charge of the surrounding monomers, which is not included in model B2.

Figure 7 shows the average frequency shift and corresponding standard deviation due to the side chain only for S1 and S2.

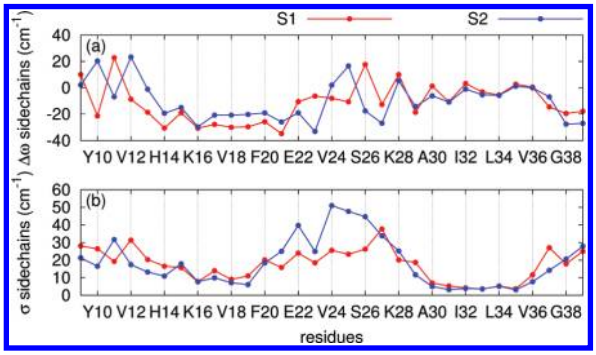

Figure 7. Average frequency shift (a) and corresponding standard deviation (b) due to the side chains only for all amide-I local modes along the peptide. (red line) system S1, (blue line) system S2.

Except in the region between residues K28 and V36, strong differences appear between systems S1 and S2. The region K28−V36 is located in the interior of the fibril and does not have any nearby Asp or Glu residues. We also notice that the standard deviation of system S2 in the loop region is much stronger than for system S1.

$\langle \Delta\omega \rangle$ and σ due to the peptide are shown in Figure 8. They are computed as the sum of the backbone contribution using model B2 and the side chain contribution for both S1 (Figure 8a,c) and S2 (Figure 8b,d). Overall, the standard deviation of the frequency shift due to the peptide has a "W" pattern similar

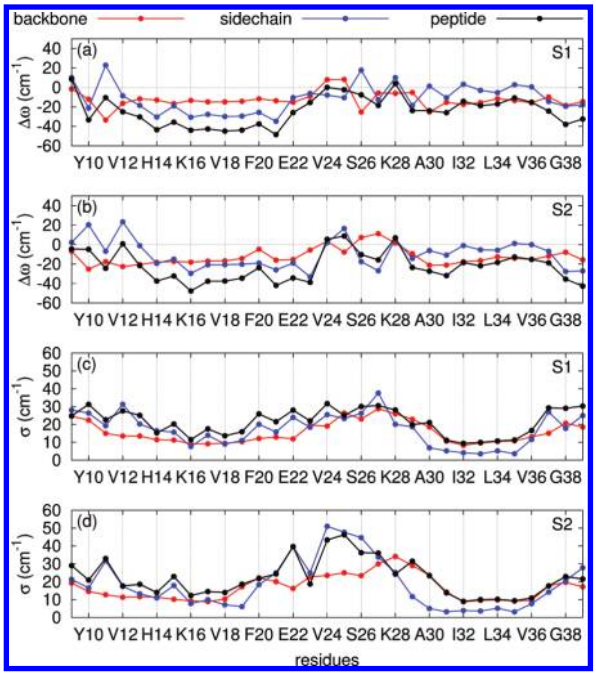

Figure 8. Average frequency shift (a,b) and corresponding standard deviation (c,d) for system S1 (a,c) and for system S2 (b,d) due to the peptide (black line), side chains (blue line), and backbone (red line). The backbone contribution is computed using the model B2.

to what has been observed in experiment and simulation on similar amyloid fibrils.[29] By comparing the side chain to the peptide contribution in Figure 8, we find that both curves have a similar behavior. This indicates that most of the inhomogeneity of the frequency distribution inside the fibril is due to the side chains and that the backbone mainly induces an overall shift of the band. Since both side chain and backbone contributions to the shift are correlated, the standard deviation of the frequency shift due to the monomers is not a simple sum of both contributions. In a similar fashion as for the average shift, the inhomogeneity is dominated by the side chain contribution. Consequently, Figure 8 shows that the frequency distribution heavily depends on the side chains.

2D-IR MEASUREMENTS AND SIMULATIONS

Details of the 2D-IR experimental setup, sample preparation, and methodology are described in refs 19−21. The grown fibrils were allowed to dry, and the final sample contained approximately 1.2 water molecules per strand.[21] Since the experimental conditions correspond to a low level of hydration, as a first step we compare the experimental measurements with our solvated Aβ40 model but excluding the water contribution to the spectral shift. Figure 9 depicts the semidiagonal traces of 2D-IR spectra of various isotopomers as described in ref 20. These traces directly characterize the absorption of each residue inside the fibrils.

The central frequency and line shape of a 2D-IR spectrum depend on the frequency distribution, the fluctuations time scale via the motional narrowing effect, and the dipole−dipole coupling. However, to compare the quality of models S1 and S2, we only focus on the frequency distribution and its inhomogeneity. Figure 9 shows the frequency distribution of model S1 and S2 using a central band of 1600 cm^{-1} and including the backbone contribution to the spectral shift using model B2 and the side chain contribution. In each spectrum we have adjusted the norm of the frequency distribution to compare with the semidiagonal traces.

Figure 9 shows that the frequency distribution of residues G29, I31, I32, G33, L34, and V36 for S1 and S2 are similar and in agreement with the experimental absorption. For G37, a strong experimental absorption is observed in the range 1575−1600 cm^{-1}. The calculation shows a band in the 1550−1600 cm^{-1} frequency range for S2 and a 1530−1570 cm^{-1} band for S1. This result indicates that most likely the experimental protonation state of side chains close to G37 should be neutral. For G25 we find a series of small peaks between 1540 cm^{-1} and 1580 cm^{-1}. It is remarkable that our S2 calculation reproduces this broad absorption. For F20, model S2 with a frequency distribution centered around 1570 cm^{-1} appears to be in a better agreement with experiment than model S1 with a frequency distribution centered around 1550 cm^{-1}. For the other residues, our model fails to reproduce the measured absorption band frequencies. Figure 9 shows that model S2 is in better agreement than S1 with experiment. Note that during the fibril growth, the amyloid is placed into a low pH environment before evaporation. This could suggest that the side chains are protonated, as in model S2.

On the basis of this result, we have simulated 2D-IR spectra of Aβ40 using S2. We have used the nonlinear exciton propagation formalism developed in ref 55 and based on the vibrational exciton picture. We have limited our calculation to the subspace of isotope labeled amide-I vibration and neglected their coupling with the main nonisotope labeled amide-I band.

dx.doi.org/10.1021/jp2096423 | J. Phys. Chem. B 2012, 116, 3322−3330

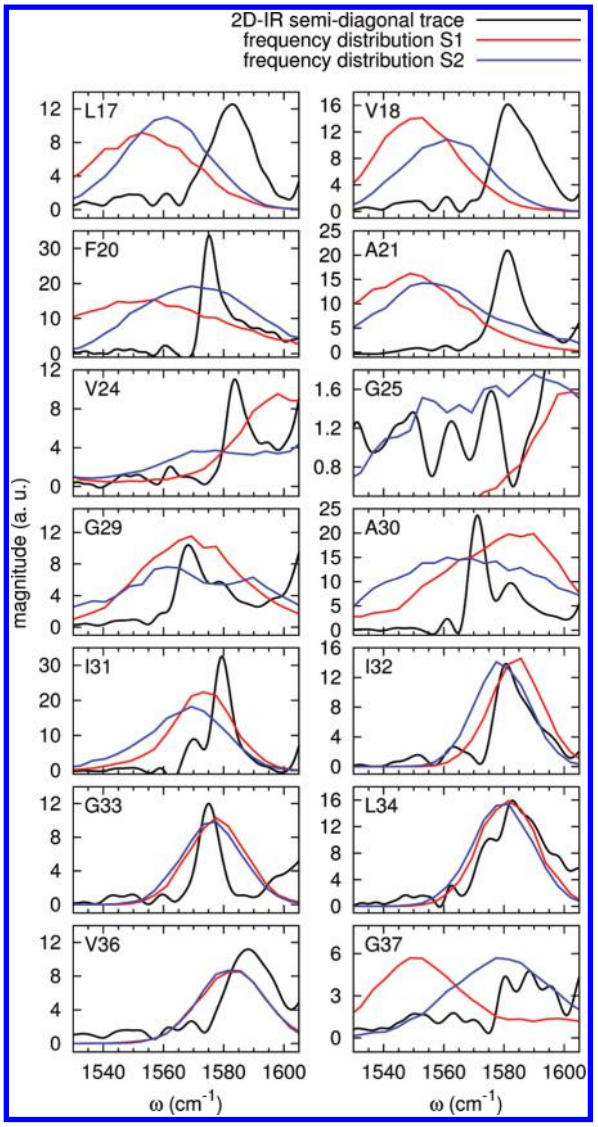

Figure 9. Semidiagonal traces of experimental 2D-IR spectra (black) of various isotopomers. Theoretical frequency distribution for systems S1 (red) and S2 (blue) using a central band of 1600 cm^{-1} and including the backbone contribution to the spectral shift using model B2 as well as the side chain contributions.

Each monomer contains one isotope-labeled amide-I vibration. Using the bosonic creation and annihilation operator of a vibrational exciton $B_i^\dagger$ and B_i on the monomer i, the model Hamiltonian is

$$H(t) = \sum_{i=1}^{N} \hbar\omega_i(t) B_i^\dagger B_i + \sum_{i,j=1}^{N} \hbar J_{ij}(t) B_i^\dagger B_j - \sum_{i=1}^{N} \hbar \frac{\Delta_i}{2} B_i^{\dagger 2} B_i^2 \quad (9)$$

where $\omega_i(t)$ is the fundamental frequency of the local isotope-labeled amide-I vibration of monomer i computed in the previous section, $J_{ij}(t)$ is the coupling between the amide-I mode of monomer i with the amide-I mode of monomer j, and Δ_i is the anharmonicity of each local mode. The sums in eq 9 run over the total number of monomers, ca. in our simulation $N = 12$. The coupling with the electric field $\boldsymbol{E}(t)$ of the laser pulses is

$$H' = \sum_i \boldsymbol{\mu}_i(t) \cdot E(t) (B_i + B_i^\dagger) \quad (10)$$

where $\boldsymbol{\mu}_i(t)$ is the transition dipole moment of the amide-I mode of ith monomer. The coupling coefficients $J_{ij}(t)$ are calculated using the transition dipole coupling (TDC) model[56] and periodic boundary conditions. The geometry and the amplitude (2.73 $D.Å^{-1}.amu^{-1/2}$) of the transition dipole moment of amide-I vibrational modes are taken from ref 56. The amide-I vibration anharmonicity is fixed to the value of 16 cm^{-1} typical for peptides.[57] To compute the spectra from this Hamiltonian, 300 trajectories of 10 ps length were harvested in the last 10 ns range of our MD simulation using a 1 fs time step. For each trajectory, the signal was generated following the simulation protocol in ref 55. The signal $S(t_1,t_2,t_3)$ was computed for $t_2 = 0$ and t_1 and t_3, varying from 0 to 10 ps. An *ad hoc* vibrational lifetime of 1.5 ps is included in our simulations. The final signal was computed as the average of the 300 trajectories. Orientational averaging was performed by summing the signal of 21 orientations following the procedure described in ref 58. Both the experiment and simulations used laser pulses with polarization in the same directions.

Figure 10 compares the experimental 2D-IR (left column) and corresponding simulations for various isotopomers. We report the signal without (central column) and with the water contribution (right column). For L17 and V18, our simulations both with and without water show a line shape considerably narrower than experiment. Our frequency distribution (see Figure 9) was much broader than in the 2D-IR spectra. This variation is due to the fast time scale of the fluctuations, which induce motional narrowing of the band. The experimental spectra show a strong inhomogeneous broadening that is missed by the structural assumptions in our simulation. For F20, the experimental 2D-IR has a main band near 1575 cm^{-1}, which tails off the high frequency side of the band. A similar shape is observed in our simulation without the water contribution. This asymmetric shape is typical for disordered one-dimensional excitons. Indeed, the simulation with water shows several distinct peaks in the high frequency region, suggesting that the peptide linkages are strongly disordered. For residue A21, the simulation with the water shows two separate bands, while the simulation without the water shows a single band similar to the experimental spectra. This suggests that residues F20 and A21 are isolated from any water molecules. For residues V24, the experimental spectrum shows a single narrow band near 1585 cm^{-1} with a high frequency tail. Our simulations show a broader spectrum both with and without the water contribution. For G25, the experimental 2D-IR shows a broad absorption with multiple peaks between 1540 cm^{-1} and 1580 cm^{-1}. The simulation yields a similar broad band between 1560 cm^{-1} and 1590 cm^{-1}. For residue G29, a good agreement is found between experiment and the simulation without the water contribution. Both spectra show a band around 1565 cm^{-1}, again with a tail in the high frequency side, typical of a quasi-linear exciton. As for F20 and A21, this suggests that no water molecules are close to the amide-I mode of G29. A similar conclusion holds for residues A30 and I31. However for residues I32, G33, L34, and V36, the theoretical spectra with and without the water are very similar and show a single and very narrow homogeneous band. Note

dx.doi.org/10.1021/jp2096423 | J. Phys. Chem. B 2012, 116, 3322–3330

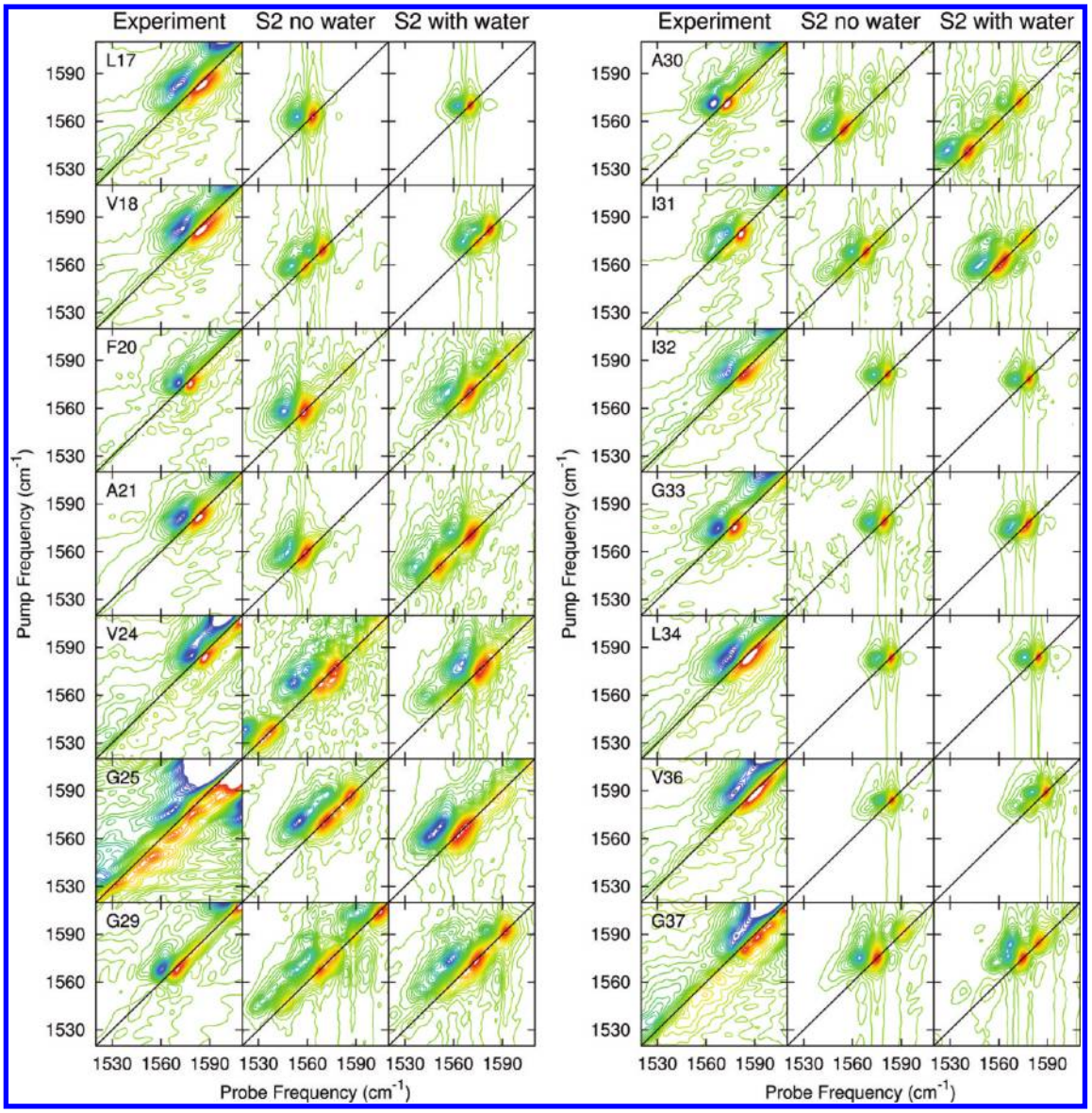

Figure 10. 2D-IR spectra of various isotopomers. Left column: experiment. Central column: simulation without the water contribution in the frequency shift. Right column: simulation including the water contribution. All simulations used a central band of 1610 cm^{-1}.

that during our simulation no water molecules were found close to these residues. The experimental spectra for I32 and G33 correspond to such situations. However L17, V18, L34, and V36 all show strong inhomogeneous contributions that must correspond to slow fluctuations between multiple structures. For residue G37, the experimental 2D-IR shows a series of peaks between 1580 cm^{-1} and 1595 cm^{-1}. The simulations, both with and without water, also show multiple peaks that must arise from structural distortions of the linear array of amide-I transitions.

CONCLUSION

We have constructed two molecular models for amyloid fibrils $A\beta_{1-40}$ based on the 2-fold symmetry NMR minimized structure of Tycko and co-workers. System S1 was built using the ionized protonation state of residue Asp and Glu, while system S2 was built with the neutral states. Our MD simulations performed without any constraints show a stable structure for S2 on the simulation time scale (25 ns). We have used these trajectories to compute the amide-I frequency distribution along the fibril using a frequency map developed by Cho and co-workers. By decomposing the frequency shift into three contributions—water, backbone, and side chains—we found that the vibrational frequency distributions inside the fibrils are dominated by the side chain fluctuations. It has been recognized for some time that inhomogeneous fluctuations of the amide-I frequency are related to the close environment. For example, in membrane peptide bundles, inhomogeneous IR line widths are larger near the edge of the membrane because of the presence of lipid head groups and water molecules.[25−28] Similarly, in our simulation we found that the side chain inhomogeneity is a main contributor to the frequency fluctuations. A set of 2D-IR semidiagonal traces were measured experimentally for 18 isotopomers following the procedure described in refs 19−21 and compared with simulated frequency distributions. The simulations based on the S2 structure are in good agreement with the experimental semidiagonal traces for residues G25, G29, I31, I32, G33, L34, V36, and G37. Using the same model, we have performed simulation of 2D-IR spectra using the excitonic picture and the

dx.doi.org/10.1021/jp2096423 | J. Phys. Chem. B 2012, 116, 3322−3330

nonlinear exciton propagation protocol.[55] Comparing simulations with and without the water contribution to the frequency fluctuations, we find that interaction with the water molecules strongly modify the 2D-IR spectra. The most homogeneous transitions in the simulated 2D-IR have the smallest effect of water, as is clearly shown in Figure 10 from the simulations for residues L17, I32, G33, and L34. The splitting of some isotopologue spectra is seen in both theory and experiment. For example, G25, G29, A30, I31, and G37 show multiple peaks in the frequency distributions in both the experiment and the simulation. In the simulations, these peaks appear whether or not water is present. Further investigations, which correlate structure and frequency, need to be performed to assign these peaks to specific structural features. In the simulation, water molecules were unable to penetrate into the fibrils in the regions of L17, V18, L34, and V36 (see Figure 2d), and the simulated 2D-IR spectra show homogeneous broadened peaks for these residues. By contrast, the experiment shows inhomogeneously broadened peaks for this group of residues. Although the experiment was performed on dry amyloid fibrils, evidence of trapped water molecules inside the fibrils near the residues L17, V18, L34, and V36 was deduced from ultrafast decay of the frequency correlation function.[21] Even though our MD simulation did not allow water molecules near these residues, the strong difference in shape between the simulated and the measured 2D-IR reinforces the suggestion that water molecules have somehow penetrated these regions. The regions where the experiments indicated the presence of mobile water molecules were recognized to consist of hydrophobic residues, and therefore it was suggested that the water may have been trapped during the formation of the fibrils. By construction, our MD simulation excludes the presence of water molecules in equilibrium in the neighborhood of these residues, supporting the conjecture of there being nonequilibrium water configurations. A recent MD study[59] on the $A\beta_{37-42}$ fibril formation, modeled by two β-sheets approaching each other, concluded that the expulsion of water molecules from the region between the sheets occurs simultaneously with the association of the two sheets, on the nanosecond time scale. However, it is conceivable that water molecules might become trapped in between or inside the β-sheets of the much larger structure of $A\beta_{1-40}$, thereby causing local deformations in the hydrogen bond network. Appropriate modifications of the amyloid model and simulation procedure that allows for the presence of long-term water molecules inside the fibril will form the subject of future work.

AUTHOR INFORMATION

Corresponding Author

*E-mail: cyril.falvo@u-psud.fr.

Notes

The authors declare no competing financial interest.

ACKNOWLEDGMENTS

We are thankful to R. Tycko for providing the amyloid fibrils structures. We gratefully acknowledge the support of the National Institutes of Health (Grant GM059230 and GM091364 to S.M. and GM12592 and PO1RR001348 to R. M. H.), and the National Science Foundation (Grant CHE-1058791 to S.M.).

REFERENCES

(1) Selkoe, D. J. *Annu. Rev. Cell Biol.* **1994**, *10*, 373−403.
(2) Tycko, R. *Curr. Opin. Struct. Biol.* **2004**, *14*, 96−103.
(3) Caughey, B.; Lansbury, P. T. *Annu. Rev. Neurosci.* **2003**, *26*, 267−298.
(4) Sunde, M.; Blake, C. C. F. *Q. Rev. Biophys.* **1998**, *31*, 1.
(5) Lester-Coll, N.; Rivera, E. J.; Soscia, S. J.; Doiron, K.; Wands, J. R.; de la Monte, S. M. *J. Alzheimer's Dis.* **2006**, *9*, 13−33.
(6) Ferreira, S. T.; Vieira, M. N. N.; De Felice, F. G. *IUBMB Life* **2007**, *59*, 332−345.
(7) Eanes, E. D.; Glenner, G. G. *J. Histochem. Cytochem.* **1968**, *16*, 673−677.
(8) Petkova, A. T.; Ishii, Y.; Balbach, J. J.; Antzutkin, O. N.; Leapman, R. D.; Delaglio, F.; Tycko, R. *Proc. Natl. Acad. Sci. U.S.A.* **2002**, *99*, 16742−16747.
(9) Petkova, A. T.; Leapman, R. D.; Guo, Z.; Yau, W.-M.; Mattson, M. P.; Tycko, R. *Science* **2005**, *307*, 262−265.
(10) Petkova, A. T.; Yau, W.-M.; Tycko, R. *Biochemistry* **2006**, *45*, 498−512.
(11) Paravastu, A. K.; Petkova, A. T.; Tycko, R. *Biophys. J.* **2006**, *90*, 4618−4629.
(12) Paravastu, A. K.; Leapman, R. D.; Yau, W.-M.; Tycko, R. *Proc. Natl. Acad. Sci. U.S.A.* **2008**, *105*, 18349−18354.
(13) Buchete, N.-V.; Tycko, R.; Hummer, G. *J. Mol. Biol.* **2005**, *353*, 804−821.
(14) Buchete, N.-V.; Hummer, G. *Biophys. J.* **2007**, *92*, 3032−3039.
(15) Mukamel, S. *Annu. Rev. Phys. Chem.* **2000**, *51*, 691−729.
(16) Zhuang, W.; Hayashi, T.; Mukamel, S. *Angnew. Chem., Int. Ed.* **2009**, *48*, 3750−3781.
(17) Volkov, V. V.; Chelli, R.; Zhuang, W.; Nuti, F.; Takaoka, Y.; Papini, A. M.; Mukamel, S.; Righini, R. *Proc. Natl. Acad. Sci. U.S.A.* **2007**, *104*, 15323−15327.
(18) Wang, J.; Chen, J.; Hochstrasser, R. M. *J. Phys. Chem. B* **2006**, *110*, 7545−7555.
(19) Kim, Y. S.; Hochstrasser, R. M. *J. Phys. Chem. B* **2009**, *113*, 8231−8251.
(20) Kim, Y. S.; Liu, L.; Axelsen, P. H.; Hochstrasser, R. M. *Proc. Natl. Acad. Sci. U.S.A.* **2008**, *105*, 7720−7725.
(21) Kim, Y. S.; Liu, L.; Axelsen, P. H.; Hochstrasser, R. M. *Proc. Natl. Acad. Sci. U.S.A.* **2009**, *106*, 17751−17756.
(22) Shim, S.-H.; Strasfeld, D.; Ling, Y.; Zanni, M. *Proc. Natl. Acad. Sci. U.S.A.* **2007**, *104*, 14197−14202.
(23) Shim, S.-H.; Gupta, R.; Ling, Y. L.; Strasfeld, D. B.; Raleigh, D. P.; Zanni, M. T. *Proc. Natl. Acad. Sci. U.S.A.* **2009**, *106*, 6614−6619.
(24) Ling, Y. L.; Strasfeld, D. B.; Shim, S.-H.; Raleigh, D. P.; Zanni, M. T. *J. Phys. Chem. B* **2009**, *113*, 2498−2505.
(25) Lin, Y.-S.; Shorb, J. M.; Mukherjee, P.; Zanni, M. T.; Skinner, J. L. *J. Phys. Chem. B* **2009**, *113*, 592−602.
(26) Woys, A. M.; Lin, Y.-S.; Reddy, A. S.; Xiong, W.; de Pablo, J. J.; Skinner, J. L.; Zanni, M. T. *J. Am. Chem. Soc.* **2010**, *132*, 2832−2838.
(27) Manor, J.; Mukherjee, P.; Lin, Y.-S.; Leonov, H.; Skinner, J. L.; Zanni, M. T.; Arkin, I. T. *Structure* **2009**, *17*, 247−254.
(28) Mukherjee, P.; Krummel, A. T.; Fulmer, E. C.; Kass, I.; Arkin, I. T.; Zanni, M. T. *J. Chem. Phys.* **2004**, *120*, 10215−10224.
(29) Wang, L.; Middleton, C. T.; Singh, S.; Reddy, A. S.; Woys, A. M.; Strasfeld, D. B.; Marek, P.; Raleigh, D. P.; de Pablo, J. J.; Zanni, M. T.; Skinner, J. L. *J. Am. Chem. Soc.* **2011**, *133*, 16062−16071.
(30) Middleton, C. T.; Buchanan, L. E.; Dunkelberger, E. B.; Zanni, M. T. *J. Phys. Chem. Lett.* **2011**, *2*, 2357−2361.
(31) Ganim, Z.; Chung, H. S.; Smith, A. W.; DeFlores, L. P.; Jones, K. C.; Tokmakoff, A. *Acc. Chem. Res.* **2008**, *41*, 432−441.
(32) Kolano, C.; Helbing, J.; Kozinski, M.; Sander, W.; Hamm, P. *Nature* **2006**, *444*, 469−472.
(33) Hamm, P.; Helbing, J.; Bredenbeck, J. *Annu. Rev. Phys. Chem.* **2008**, *59*, 291−317.
(34) Roy, S.; Jansen, T. L. C.; Knoester, J. *Phys. Chem. Chem. Phys.* **2010**, *12*, 9347−9357.
(35) Liang, C.; Jansen, T. L. C.; Knoester, J. *J. Chem. Phys.* **2011**, *134*, 044502−8.

(36) Kalé, L.; Skeel, R.; Bhandarkar, M.; Brunner, R.; Gursoy, A.; Krawetz, N.; Phillips, J.; Shinozaki, A.; Varadarajan, K.; Schulten, K. *J. Comput. Phys.* **1999**, *151*, 283−312.
(37) MacKerell, A. D. *J. Phys. Chem. B* **1998**, *102*, 3586−3616.
(38) Essmann, U.; Perera, L.; Berkowitz, M. L.; Darden, T.; Lee, H.; Pedersen, L. G. *J. Chem. Phys.* **1995**, *103*, 8577−8593.
(39) Darden, T.; York, D.; Pedersen, L. *J. Chem. Phys.* **1993**, *98*, 10089−10092.
(40) Martyna, G. J.; Tobias, D. J.; Klein, M. L. *J. Chem. Phys.* **1994**, *101*, 4177−4189.
(41) Feller, S. E.; Zhang, Y.; Pastor, R. W.; Brooks, B. R. *J. Chem. Phys.* **1995**, *103*, 4613−4621.
(42) Jorgensen, W. L.; Chandrasekhar, J.; Madura, J. D.; Impey, R. W.; Klein, M. L. *J. Chem. Phys.* **1983**, *79*, 926−935.
(43) Ham, S.; Kim, J.-H.; Lee, H.; Cho, M. *J. Chem. Phys.* **2003**, *118*, 3491−3498.
(44) Ham, S.; Cha, S.; Choi, J.-H.; Cho, M. *J. Chem. Phys.* **2003**, *119*, 1451−1461.
(45) Choi, J.-H.; Ham, S.; Cho, M. *J. Phys. Chem. B* **2003**, *107*, 9132−9138.
(46) Bour, P.; Keiderling, T. A. *J. Chem. Phys.* **2003**, *119*, 11253−11262.
(47) Jansen, T. L. C.; Knoester, J. *J. Chem. Phys.* **2006**, *124*, 044502.
(48) Bloem, R.; Dijkstra, A. G.; Jansen, T. L. C.; Knoester, J. *J. Chem. Phys.* **2008**, *129*, 055101.
(49) Schmidt, J. R.; Corcelli, S. A.; Skinner, J. L. *J. Chem. Phys.* **2004**, *121*, 8887−8896.
(50) Auer, B. M.; Skinner, J. L. *J. Chem. Phys.* **2008**, *128*, 224511.
(51) Zhuang, W.; Abramavicius, D.; Hayashi, T.; Mukamel, S. *J. Phys. Chem. B* **2006**, *110*, 3362−3374.
(52) Falvo, C.; Hayashi, T.; Zhuang, W.; Mukamel, S. *J. Phys. Chem. B* **2008**, *112*, 12479−12490.
(53) Paarmann, A.; Hayashi, T.; Mukamel, S.; Miller, R. J. D. *J. Chem. Phys.* **2008**, *128*, 191103.
(54) Bagchi, S.; Falvo, C.; Mukamel, S.; Hochstrasser, R. M. *J. Phys. Chem. B* **2009**, *113*, 11260−11273.
(55) Falvo, C.; Palmieri, B.; Mukamel, S. *J. Chem. Phys.* **2009**, *130*, 184501.
(56) Torii, H.; Tasumi, M. *J. Raman Spectrosc.* **1998**, *29*, 81−86.
(57) Hamm, P.; Lim, M.; Hochstrasser, R. M. *J. Phys. Chem. B* **1998**, *102*, 6123−6138.
(58) Hochstrasser, R. M. *Chem. Phys.* **2001**, *266*, 273−284.
(59) Reddy, G.; Straub, J. E.; Thirumalai, D. *Proc. Natl. Acad. Sci. U.S.A.* **2010**, *107*, 21459−21464.